applied sciences

MDPI

Article

Impact of Thermal and Ultraviolet Treatments on the Structural, Mechanical, and Laser Ablation Properties of Fluorinated Ethylene Propylene Films

Brigita Abakevičienė, Algirdas Lazauskas, Viktoras Grigaliūnas and Dalius Jucius *

Institute of Materials Science, Kaunas University of Technology, Barsausko Str. 59, LT-51423 Kaunas, Lithuania; brigita.abakeviciene@ktu.lt (B.A.); algirdas.lazauskas@ktu.lt (A.L.); viktoras.grigaliunas@ktu.lt (V.G.)
* Correspondence: dalius.jucius@ktu.lt

Abstract: Fluorinated ethylene propylene (FEP) films were subjected to heat, UV, and heat–UV treatments. Structural changes that occurred after these treatments were recorded via X-ray diffraction (XRD), microtensile, and laser ablation testing. XRD macromolecular orientation texture analysis revealed changes in the fraction of crystalline components and the degree of anisotropy of the FEP films after being subjected to different processing conditions. Heat treatment at 200 °C affected structural properties by rearranging the crystallites and resulting in a higher degree of anisotropy. By contrast, the UV treatment of FEP resulted in a lower degree of anisotropy. The changes in anisotropy and crystallinity of FEP films significantly affected their Young's modulus and yield stress. The UV laser ablation threshold values were found to be lower for the heat-treated FEP films.

Keywords: material testing; fluorinated ethylene propylene; heat–UV treatment; X-ray diffraction; laser ablation

Academic Editor: Ephraim Suhir

Received: 4 April 2025
Revised: 14 April 2025
Accepted: 24 April 2025
Published: 25 April 2025

Citation: Abakevičienė, B.; Lazauskas, A.; Grigaliūnas, V.; Jucius, D. Impact of Thermal and Ultraviolet Treatments on the Structural, Mechanical, and Laser Ablation Properties of Fluorinated Ethylene Propylene Films. *Appl. Sci.* **2025**, *15*, 4796. https://doi.org/10.3390/app15094796

1. Introduction

Due to their high thermochemical stability, transmittance in the UV-VIS-IR spectral range, and resistance to aging, fluoropolymer materials have applications in various industries, including the piping, textiles, aerospace, automotive, and medical sectors [1–3]. Recently, they have begun to be applied in microelectronics and micro-optics, where they can replace micro-optical structures fabricated from expensive materials such as fused silica [4,5], or be used as nanostructured fuel cell or gas sensor membranes [6,7]. Fluoropolymers are classified into two major categories: fully fluorinated polymers (e.g., polytetrafluoroethylene (PTFE), perfluoroalkoxy (PFA), and fluorinated ethylene propylene (FEP)) and partially fluorinated polymers (e.g., ethylene tetrafluorothylene (ETFE), polyvinylidene fluoride (PVDF), and ethylene chlorotrifluoroethylene (ECTFE)). The high strength of the interatomic bonds and the nonpolarity of the structural components result in a high degree of crystallinity and superior performance in extreme environments of fully fluorinated polymers. However, harsh environmental or operating conditions can alter the level of crystallinity, as well as other properties [8].

Fluoropolymeric materials exhibit a complicated nonlinear response when subjected to external loads. At small deformations, the material response is linear viscoelastic. At higher strains, the material undergoes distributed yield, unrecoverable deformation, viscoplastic flow, and finally gradual stiffening at large deformations until the ultimate failure occurs [9]. Therefore, it is important to understand the effects of extreme physical

factors (e.g., heat and UV radiation) on the structural and mechanical properties and degradability of fluoropolymer materials at a micro-level scale.

FEP is a melt-processable semicrystalline copolymer of tetrafluoroethylene and hexafluoropropylene. It is a transparent and durable material widely used due to its unique chemical, mechanical, and thermal properties [10–12]. FEP films transmit more UV, visible, and infrared radiation than ordinary window glass [13]. The occasional methyl side groups attached to the backbone act as defects, reducing the melting point as well as the cold flow of the polymer. The crystallinity of molded FEP parts may vary between 30% and 50%, depending on processing conditions [14]. Thus, FEP films are particularly promising for use in the optical systems and photovoltaic industry.

Recent research on FEP films has focused on modifying their inherently inert surfaces through heat and UV treatments to enhance their functionality in advanced applications. Heat treatment, typically performed between 100 °C and 250 °C, can induce molecular rearrangement and increase crystallinity [15]. Controlled annealing may also improve adhesion by inducing minor surface restructuring or partial defluorination [16]. In contrast, UV treatment, particularly in the presence of ozone or reactive gases, promotes surface activation by breaking C–F bonds and introducing polar functional groups such as hydroxyl and carboxyl groups [17]. This modification enhances surface energy, wettability, and compatibility with coatings or biomaterials [18]. Techniques such as UV-induced photografting have been employed to functionalize FEP films with hydrophilic moieties, while exposure to UV/ozone has enabled nanostructuring for microfluidic and biomedical applications [19]. Combined heat and UV treatments have demonstrated synergistic effects in tuning surface properties for sensor interfaces and dielectric layers [20]. However, the influences of heat- and UV-induced microstructural transformations on functional performance shifts in FEP films are still underestimated and require more attention because they are relevant for applications like space materials, optics, or microfabrication.

In this work, crystallinity changes in heat–UV-treated FEP films were investigated via X-ray diffraction (XRD). The mechanical properties of FEP were evaluated through a series of tensile tests on the small-strain deformation behavior. The ablation threshold and the ablation rate of virgin and heat-treated FEP films were determined using a nanosecond UV laser. Macromolecular orientation texture analysis of heat- and UV-treated FEP revealed crystal structure differences, which correlate with the results of laser ablation and microtensile testing, showing differences in the material's elastic–plastic properties when stress was applied in different directions.

2. Materials and Methods

The samples were cut with a custom-built mechanical cutting machine from 25 µm thick FEP films (DuPontTM Teflon® FEP, Washington, WV, USA). The cutting was performed in two directions: parallel to or perpendicular to the roll direction. Small "dog-bone"-shaped samples were used for microtensile tests with an overall length of 20 mm, a gauge length of 4 mm between the heads, and a width of 1 mm in the neck region. The radius of the shoulder was R = 1 mm, which yielded a gauge length of 2 mm of a constant cross-section. The effective length (L_{eff}) that corresponds to the length of an equivalent sample having a constant cross-section in between the two sample heads was 3.515 mm [21].

The virgin samples (FEP-1) were subjected to heat treatment (FEP-2) for 30 min at a temperature of 200 °C (close to the maximum operating temperature) on a programmable POLOS Hotplate 200S (SPS, Bienenbüttel, Germany) with a uniform temperature of ±0.5 °C; UV exposure (FEP-3) using the ABA class collimated solar simulator SF150B (Sciencetech Inc., London, ON, Canada), equipped with a Xenon short-arc lamp; and AM1.5G filter

(irradiance—1.13 mW/cm^2 @ 254 nm and 3 mW/cm^2 @ 365 nm, exposure time—72 h), as well as the combination of heat treatment and UV exposure (FEP-4).

X-ray diffraction data were collected using a D8 Discover X-ray diffractometer (Bruker AXS GmbH, Karlsruhe, Germany) with a Cu K_α (λ= 1.54 Å) X-ray source. Parallel beam geometry with a 60 mm Göbel mirror (i.e., an X-ray mirror on a high-precision parabolic surface) was used. This configuration enables the divergent incident X-ray beam to be transformed from a line focus of the X-ray tube into a parallel beam that is free of K_β radiation. The primary side also had a Soller slit with an axial divergence of 2.5°. The secondary side had a LYNXEYE (1D mode) detector with an opening angle of 2.160° and a slit opening of 6.0 mm. The voltage and current of the X-ray generator were 40.0 kV and 40 mA, respectively. Coupled $2\theta/\theta$ scans were performed in the range of 3.0–30.0° with a step size of 0.016°, a time per step of 19.2 s, and an auto-repeat function enabled. The processing of the resultant diffractograms was performed with DIFFRAC.EVA V7 software. Macromolecular orientation texture analysis was performed to describe the variation in pole density (determined by the intensity of the diffracted X-ray beam) with pole orientation for crystalline component reflection at 17.69° in 2θ. Data were collected using a standard mode (unlocked coupled) with 5° of δ measured for a full circle 0–360 incr. 5° in the Phi (φ) range and 0–60 incr. 10° in the Psi (ψ) range. The measured data were corrected for background scattering and beam defocus using the Diffrac^{plus} MULTEX 3 software package.

The mechanical properties of the FEP film samples were investigated with a custom-built tripod design uniaxial microtensile tester, which is described in previous work [22]. The piezo-actuated microtensile setup was able to measure film elongation up to 210 µm with an accuracy of 50 nm. The total strain applied during the tensile tests was 5%. The strain rate of the tensile experiments was 4.8 µm/s. The registration of the force and displacement of the samples was carried out during the tensile tests. The force of tension was applied parallel and perpendicular to the principal orientation direction of the FEP films. During the tensile test, five samples were investigated for each different processing condition. Each sample was loaded and unloaded, and the mean values of Young's modulus and yield stress were obtained as an average of five tested samples. Values are reported as means ± standard error of the mean.

In the experiments, an industrial-grade diode-pumped solid-state UV laser (Baltic HP, Ekspla, Vilnius, Lithuania) with a pulse duration of ~10 ns emitting at a wavelength of 355 nm was used. The laser provided light pulses with pulse energy up to 50 µJ at a repetition rate of 20 kHz with an average laser power of 1 W. The laser power was controlled using an external attenuator, which consisted of a polarizing beam splitter cube, a half-wave phase plate, and the beam trap. The beam was expanded using a telescope composed of concave and convex lenses. The beam expander was used to vary the beam diameter on the objective lens and adjust the spot's size on the sample. The beam position on the sample was controlled via a galvanometer scanner (Scancube 10, Scanlab, Puchheim, Germany). The f-theta objective lens with a focal length of 174 mm was used to focus the beam on the surface of the target material. The radius of the transverse focal spot on the sample's surface was measured using the technique described in [23], which was $w_0 \approx 20$ µm.

The diameters D of the laser-ablated areas were measured with an optical microscope. The laser fluence sufficient to ablate the material for a fixed number of laser pulses per spot N is denoted as the ablation threshold fluence $F_{th}(N)$. Assuming that a laser beam has the Gaussian spatial beam profile, the relationship between the diameter of the crater D and the peak laser fluence $F_0 = 2E_p/\pi{w_0}^2$ in the center of the Gaussian beam can be written as follows [23]:

$$D^2 = 2w_0^2 \ln\left(\frac{F_0}{F_{th}(N)}\right), \quad (1)$$

where w_0 is the radius of the Gaussian beam on the sample, and E_p is the pulse energy. The incubation model describes the relationship between the single-pulse ablation threshold $F_{th}(1)$ and the multi-pulse ablation threshold $F_{th}(N)$ in the following form [24]:

$$F_{th}(N) = F_{th}(1) \cdot N^{\xi-1} \quad (2)$$

Here, ξ is a material-dependent incubation parameter. ξ = 1 means that no incubation effect is observable.

3. Results and Discussion

X-ray diffraction experiments were performed to reveal structural changes that occur under different processing conditions of the FEP polymer. Figure 1 shows the raw diffraction patterns of virgin (FEP-1), heat-treated (FEP-2), UV-treated (FEP-3), and heat–UV-treated (FEP-4) samples, as well as deconvoluted amorphous and crystalline components for each diffraction pattern, respectively. The reflection of the crystalline component remained at ~17.69° in 2θ after different FEP treatment procedures. The size of the crystallite was estimated from the reflex of the main crystalline component at 2θ ~17.69° according to the Sherrer equation [25]. Crystallite size values were found to be 235.5 Å, 232.8 Å, 233.1 Å, and 234.9 Å for FEP-1, FEP-2, FEP-3, and FEP-4, respectively. The crystalline fraction for FEP-1, FEP-2, FEP-3, and FEP-4 was determined to be 43.7%, 45.0%, 44.0%, and 44.1%, respectively. Unfortunately, the obtained results are not sufficient to reveal the full image of structural changes present in FEP after different treatments and may lead to speculative conclusions about the polymer stability and degradation processes.

To reveal the polymer chain reorganization in the FEP structure, the macromolecular orientation texture analysis was performed employing XRD via the pole figure measurements. The intensity of 2θ maxima of the crystalline component was measured by moving the sample through ψ (tilt) azimuth angle and φ (spindle) polar rotations and plotting the measured intensities in the hemisphere-like distribution of scattered intensity via orthographic projection on a pole figure. Figure 2 shows the calculated pole figures for the reflexes of the crystalline components of FEP-1, FEP-2, FEP-3, and FEP-4.

It can be clearly seen that the FEP treatment processes significantly affected the structural properties of the polymer, producing different crystalline morphologies. Through the intensity distribution analysis based on k-means clustering, the values of the crystalline fraction (denoted as C_f) were refined and displayed with each pole figure, respectively. To quantitatively estimate the degree of anisotropy from the calculated pole figures, the power spectrum method was employed for the determination of the fractal dimension (D_f). This method is based on the power spectrum dependence of the fractional Brownian motion. Every line intensity profile that forms the pole figure underwent Fourier transform analysis, and the power spectrum was evaluated and averaged. The fractal dimension was calculated from the slope β of a least-square regression line fit to the data points in the log–log plot of the power spectrum as $D_f = 7/2 - \beta/2$. In general, D_f directly correlates with the degree of anisotropy: the lower the D_f, the higher the anisotropy.

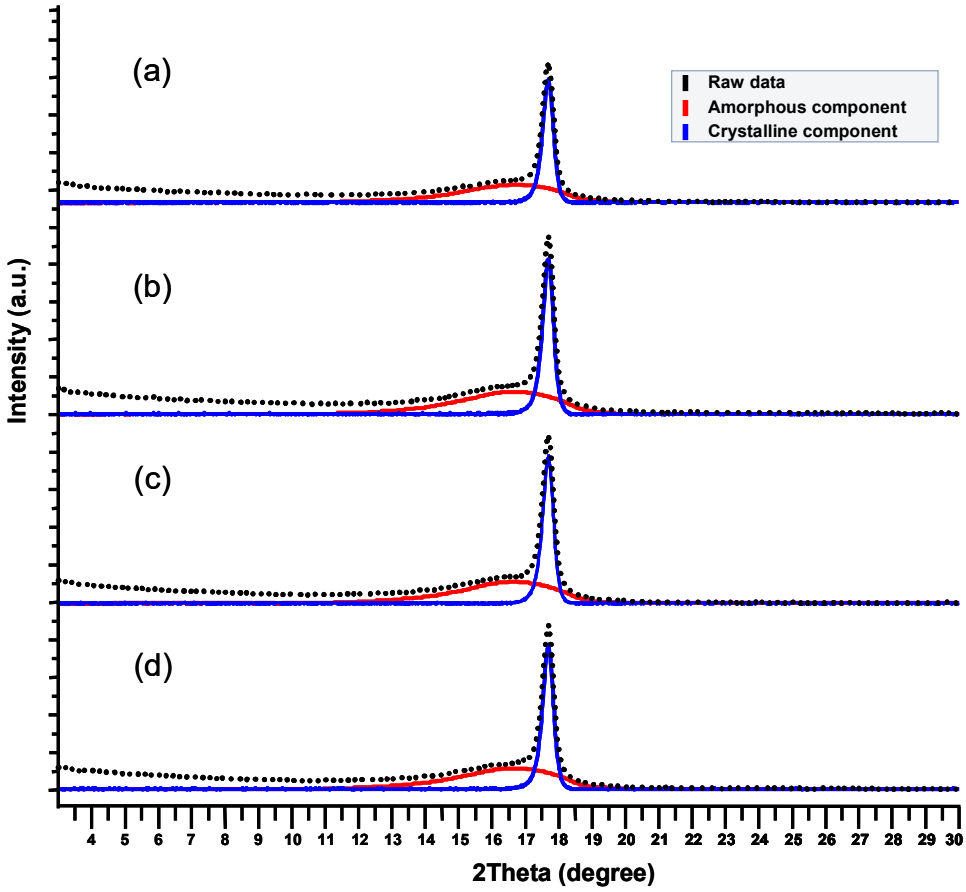

Figure 1. X-ray diffraction patterns with deconvoluted amorphous and crystalline components: (**a**) FEP-1; (**b**) FEP-2; (**c**) FEP-3; (**d**) FEP-4.

Figure 3 shows the power spectra for the pole figures $\psi = 0^\circ$ of FEP-1, FEP-2, FEP-3 and FEP-4, respectively. Based on the analysis of power spectra, the heat treatment of FEP at 200 °C (FEP-2) affected its structural properties by rearranging crystallites and resulting in the highest degree of anisotropy with a D_f value of 2.64. By contrast, the UV treatment of FEP (FEP-3) resulted in a polymer structure with the lowest degree of anisotropy ($D_f = 2.71$). For virgin FEP-1, D_f was determined to be 2.69, while after heat treatment and UV exposure (FEP-4), it was reduced to 2.67, resulting in a higher anisotropy. The increased anisotropy upon heating can be attributed to the rearrangement and alignment of crystallites facilitated by thermal energy. Conversely, the decrease in anisotropy after UV exposure is likely due to photochemical processes, such as radical generation and the oxidation of tertiary carbons linked to the perfluoromethyl groups, which disrupt the polymer chain alignment and hinder the formation of a strongly oriented structure, leading to a more isotropic state despite a potential increase in the overall crystalline fraction.

Nanosecond pulsed UV laser irradiation was used in order to determine the influence of heat treatment on the ablation parameters of FEP films. The crater diameter of laser-ablated polymers was analyzed using an optical microscope. The key ablation differences between the virgin (FEP-1) and heat-treated (FEP-3) polymers can be seen in Figure 4.

Taking into account Equation (1) with the various pulse energy values, an ablation threshold fluence *F*th is obtained from a semi-logarithmic plot of the diameter squared of the ablated area D^2 versus peak laser fluence F_0. The slope of the straight lines provides the Gaussian beam radius w_0. Figure 5 shows experimental results of the squared diameters D^2 of ablated areas versus laser fluence F_0 for laser-processed FEP polymers considering a different number of pulses per spot (N = 5, 10, 20, 30, 50, and 100).

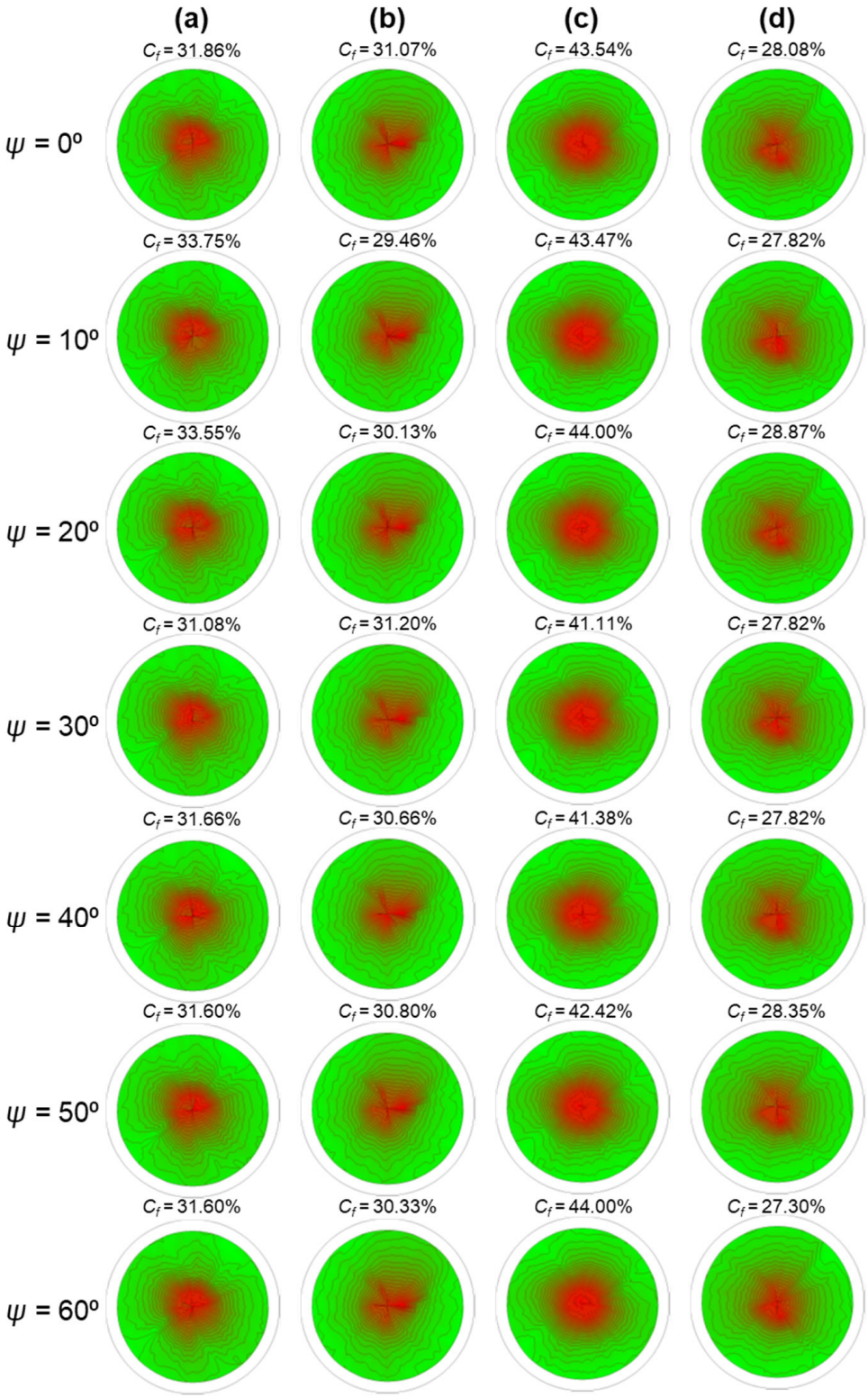

Figure 2. Calculated pole figures for crystalline component reflex: (**a**) FEP-1; (**b**) FEP-2; (**c**) FEP-3; (**d**) FEP-4.

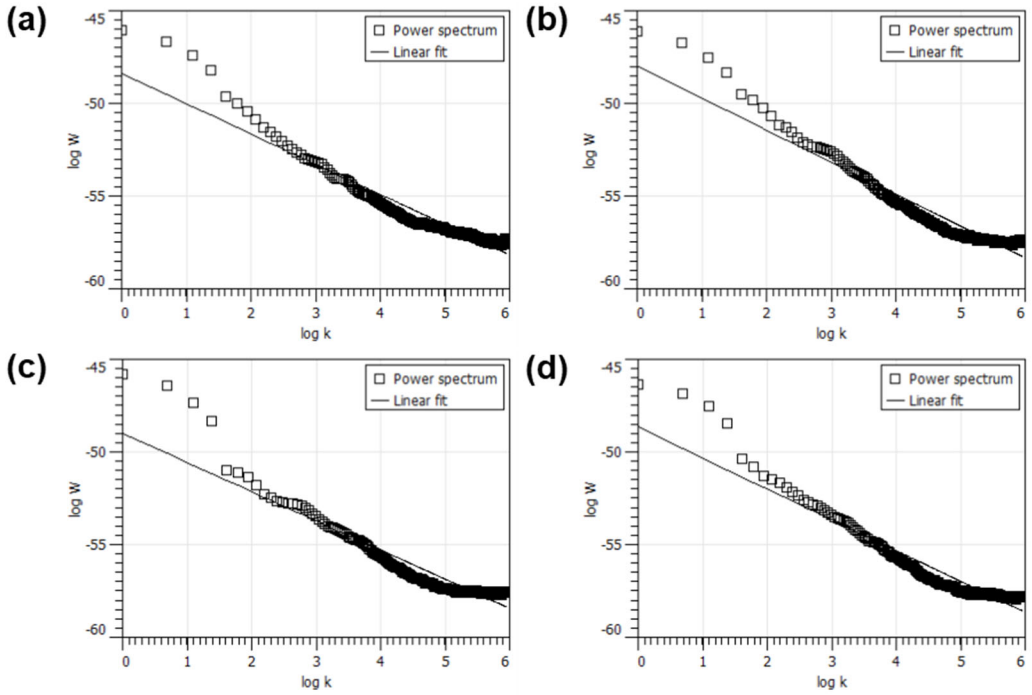

Figure 3. Power spectra for pole figures at $\psi = 0^{\circ}$: (**a**) FEP-1; (**b**) FEP-2; (**c**) FEP-3; (**d**) FEP-4.

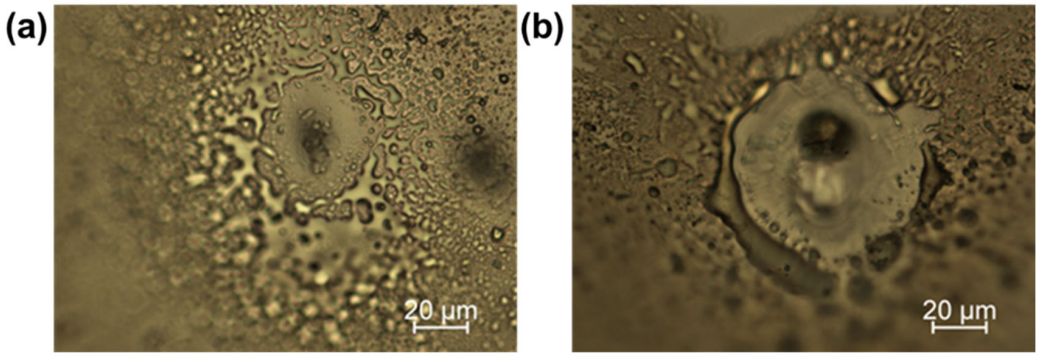

Figure 4. The optical microscope images of nanosecond pulsed laser treatment of the FEP polymer: (**a**) virgin and (**b**) heat-treated. Laser parameters: τ_p ~10 ns, λ = 355 nm and $f_{rep} \approx$ 20 kHz, N = 100 pulses per spot, pulse energy E_p = 50 μJ.

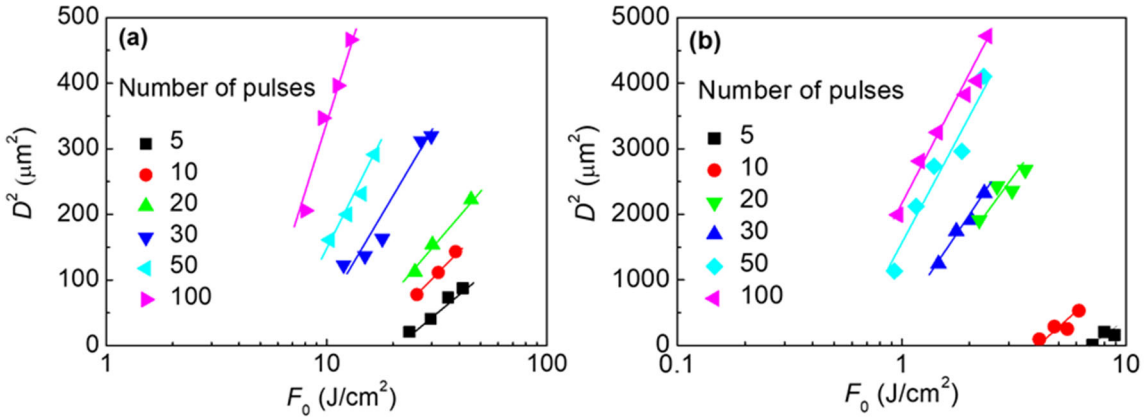

Figure 5. Nanosecond pulsed laser treatment of FEP polymer: (**a**) virgin; (**b**) heat-treated. Squared diameters of the ablated areas of the FEP polymer in dependence on the peak laser fluence in the center of the Gaussian beam. Solid symbols—experimental data points; solid lines—fit by Equation (1). Laser parameters: τ_p ~10 ns, λ = 355 nm, and $f_{rep} \approx$ 20 kHz.

Almost parallel lines with a fixed slope represent different modification thresholds for variant N due to the incubation phenomena. The extrapolation to $D^2 = 0$ gives the modification threshold fluences presented in Table 1.

Table 1. Ablation thresholds $F_{th}(N)$ of FEP polymer for a different number of laser pulses per spot. Laser parameters: τ_p ~10 ns, λ = 355 nm, and $f_{rep} \approx 20$ kHz.

N	Virgin FEP	Heat-Treated FEP
	$F_{th}(N)$, J/cm^2	$F_{th}(N)$, J/cm^2
20	9.36	1.05
30	7.84	0.88
50	5.98	0.70
100	4.28	0.51

The ablation threshold values decreased with an increase in the number of pulses. The threshold values were lower for the heat-treated FEP polymer by a factor of ~10. Figure 6 shows a graph of the accumulated laser fluence $N \times F_{th}(N)$ versus the number of pulses N for the FEP polymer.

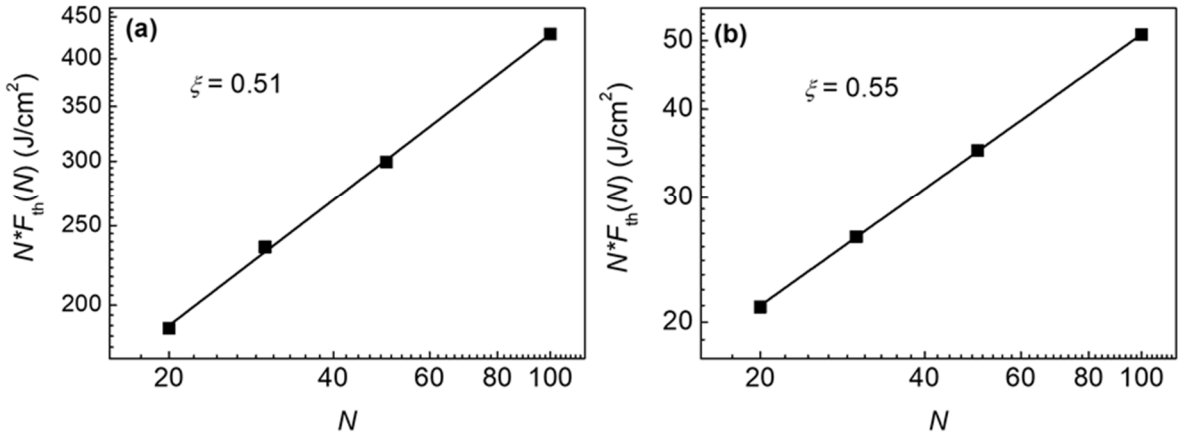

Figure 6. Multi-pulse incubation behavior of the FEP polymer: (**a**) virgin, (**b**) heat-treated. Accumulated laser fluence $N \times F_{th}(N)$ versus number of laser pulses per spot N. Solid symbols—experimental data points; solid lines—fit by Equation (2). Laser parameters: τ_p ~10 ns, λ = 355 nm, and $f_{rep} \approx 20$ kHz.

Potential sources of error in determining ablation thresholds include thermal accumulation, uncertainties in crater measurements due to polymer swelling or re-deposition, and deviations from an ideal Gaussian beam profile, which we estimated could lead to a 10% discrepancy between the calculated and actual ablation thresholds. However, the overall trends, including the decrease in threshold fluence with pulse number and differences between the virgin and heat-treated FEP, remained consistent with the established polymer ablation behavior.

Virgin (FEP-1) as well as heat (FEP-2)-, UV light (FEP-3)-, and heat–UV (FEP-4)-treated 25 μm thick FEP polymer samples of two different rolling directions were tested in the microtensile setup to determine Young's modulus E (slope of the tangent to the stress–strain curve) and yield stress $\sigma_{y0.2}$ (at 0.2% of strain ε). The average stress–strain curves for each FEP sample cut in parallel and perpendicular to the roll direction of the polymer are presented in Figures 7 and 8, respectively. The characteristic solid tangential line represents the determination of Young's modulus for the UV light-affected sample. The intersection of the dashed line with the experimental curve at a 0.2% strain offset provides the yield stress ($\sigma_{y0.2}$).

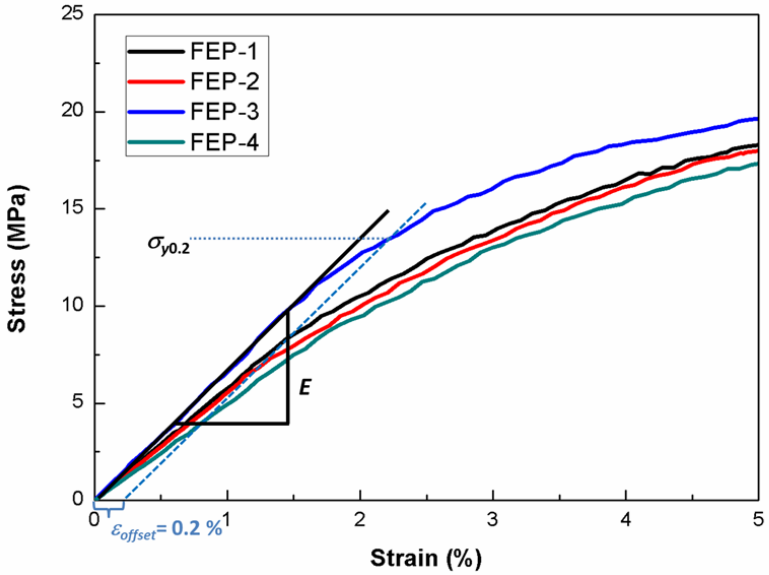

Figure 7. Stress–strain curves for FEP samples cut in parallel to the roll direction: virgin (FEP-1) as well as heat (FEP-2)-, UV light (FEP-3)-, and heat–UV (FEP-4)-affected films.

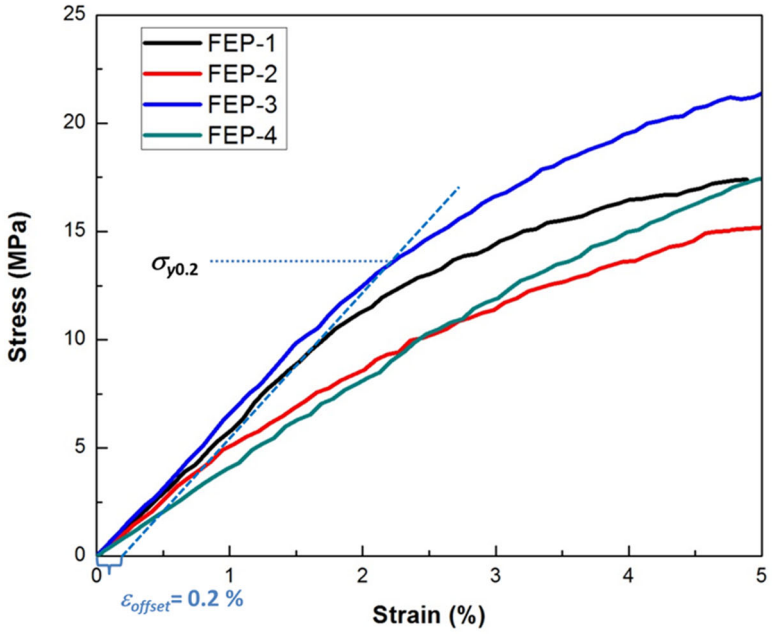

Figure 8. Stress–strain curves for FEP samples cut perpendicular to the roll direction: virgin (FEP-1) a well as heat (FEP-2)-, UV light (FEP-3)-, and heat–UV (FEP-4)-affected films.

Young's modulus and yield stress values are summarized in Table 2. From the experimental stress–strain curves, it can be observed that the FEP samples had a linear elastic behavior below strains of 1.5%. Extrapolating linear elastic parts of the experimental stress–strain curves of virgin FEP-1 samples with two different cutting directions of the polymer, we found mean Young's modulus values of 583.92 ± 0.23 MPa and 589.46 ± 0.21 MPa and mean yield stress values of 11.60 ± 0.10 MPa and 12.17 ± 0.07 MPa for samples cut parallel and perpendicular to the FEP roll direction, respectively. Young's modulus and yield stress of heat-treated FEP films (FEP-2) with different cutting directions decreased slightly from 555.57 MPa to 511.19 MPa, and from 10.92 MPa to 10.36 MPa, respectively. The changes in mechanical properties, as well as differences in Young's modulus and yield stress for the two different cutting directions of the heat-treated FEP samples, could be associated with an increase in the anisotropy of the films. Certain rearrangements of

polymer chains caused a slight reduction in the fraction of crystalline polymer components from 31.86% to 31.07% (see Figure 2a,b). UV light-treated FEP films (FEP-3) showed a moderate increase in the fraction of crystalline components (43.54%), Young's modulus (651.88–665.52 MPa), and yield stress (12.89–13.31 MPa) for both cutting directions. The increase in the fraction of the crystalline component and the decrease in anisotropy could be associated with the generation of radicals and the oxidation of tertiary carbon, which is bonded to the perfluoromethyl group responsible for the amorphicity of the FEP film. As the crystalline regions in the polymer became more refined, the possibilities for stress concentration in less cohesive amorphous regions significantly decreased, which led to enhanced mechanical properties compared to those of the more amorphous polymer. The decrease in crystalline component fraction (28.08%), Young's modulus (408.62–499.11 MPa), and yield stress (8.39–9.69.MPa) of heat–UV-treated FEP films (FEP-4) for both cutting directions could be due to polymer chain rearrangement, which is a complex function of combined treatment.

Table 2. Young's modulus (E) and yield stress ($\sigma_{y0.2}$) values. The notation represents the "±" standard error of the mean.

Sample		E (MPa)	$\sigma_{y0.2}$ (MPa)
Parallel to the FEP roll direction	FEP-1	583.92 ± 0.23	11.60 ± 0.10
	FEP-2	555.57 ± 0.32	10.92 ± 0.12
	FEP-3	665.52 ± 0.13	13.31 ± 0.08
	FEP-4	499.11 ± 0.43	9.69 ± 0.12
Perpendicular to the FEP roll direction	FEP-1	589.46 ± 0.21	12.17 ± 0.07
	FEP-2	511.19 ± 0.35	10.36 ± 0.13
	FEP-3	651.88 ± 0.12	12.89 ± 0.07
	FEP-4	408.62 ± 0.50	8.39 ± 0.13

4. Conclusions

In this study, we report on the important changes in the structure of FEP films resulting from the different treatment procedures that mimic extreme environmental conditions. Macromolecular orientation texture analysis of FEP films revealed changes in the crystalline component fraction and degree of anisotropy after exposure to heat, UV, and heat–UV treatments. The heat treatment of FEP at 200 °C affected its structural properties by rearranging the crystallites and resulting in the highest degree of anisotropy, with a D_f value of 2.64. The UV treatment of FEP resulted in a polymer structure with the lowest degree of anisotropy (D_f = 2.71). The increase in anisotropy of the FEP films also affected their mechanical properties, as well as differences in Young's modulus and yield stress. The stress concentration in less cohesive amorphous regions significantly decreased, as quantified by uniaxial microtensile testing results. Young's modulus and yield stress for UV light-treated FEP films were found to be highest with the obtained values of 651.88–665.52 MPa and 12.89–13.31 MPa, respectively. The structural changes that occurred were further quantified via laser ablation tests. The laser ablation threshold values were found to be lower for the heat-treated FEP polymer by a factor of ~10.

Author Contributions: Conceptualization, A.L. and V.G.; methodology, B.A., A.L. and D.J.; validation, B.A. and D.J.; formal analysis, D.J.; investigation, B.A., A.L., V.G. and D.J.; resources, V.G.; data curation, B.A. and A.L.; writing—original draft preparation, B.A., A.L., V.G. and D.J.; writing—review and editing, D.J.; visualization, B.A. and A.L.; supervision, V.G.; project administration, V.G. All authors have read and agreed to the published version of the manuscript.

Funding: This research received no external funding.

Institutional Review Board Statement: Not applicable.

Informed Consent Statement: Not applicable.

Data Availability Statement: The original contributions presented in this study are included in the article. Further inquiries can be directed to the corresponding author.

Conflicts of Interest: The authors declare no conflicts of interest.

References

1. Teng, H. Overview of the development of the fluoropolymer industry. *Appl. Sci.* **2012**, *2*, 496–512. [CrossRef]
2. Ameduri, B. Fluoropolymers as unique and irreplaceable materials: Challenges and future trends in these specific per or poly-fluoroalkyl substances. *Molecules* **2023**, *28*, 7564. [CrossRef] [PubMed]
3. Lv, J.; Cheng, Y. Fluoropolymers in biomedical applications: State-of-the-art and future perspectives. *Chem. Soc. Rev.* **2021**, *50*, 5435–5467. [CrossRef] [PubMed]
4. Goldenberg, L.M.; Köhler, M.; Dreyer, C. Fluorinated polymers for photonics—From optical waveguides to polymer-clad glass optical fibers. *Appl. Sci.* **2025**, *15*, 1790. [CrossRef]
5. Jucius, D.; Lazauskas, A.; Grigaliūnas, V.; Abakevičienė, B.; Smetona, S.; Tamulevičius, S. UV-NIL replication of microlens arrays on flexible fluoropolymer substrates. *Microsyst. Technol.* **2018**, *24*, 1115–1125. [CrossRef]
6. Prakash, O.; Tiwari, S.; Maiti, P. Fluoropolymers and their nanohybrids as energy materials: Application to fuel cells and energy harvesting. *ACS Omega* **2022**, *39*, 34718–34740. [CrossRef]
7. Graunke, T.; Schmitt, K.; Raible, S.; Wöllenstein, J. Towards enhanced gas sensor performance with fluoropolymer membranes. *Sensors* **2016**, *16*, 1605. [CrossRef]
8. Galante, A.M.S.; Galante, O.L.; Campos, L.L. Study on application of PTFE, FEP and PFA fluoropolymers on radiation dosimetry. *Nucl. Instrum. Methods Phys. Res. A* **2010**, *619*, 177–180. [CrossRef]
9. Bergstrom, J.S.; Hilbert, L.B., Jr. A constitutive model for predicting the large deformation thermomechanical behavior of fluoropolymers. *Mech. Mater.* **2005**, *37*, 899–913. [CrossRef]
10. Barhoumi, N.; Khlifi, K.; Maazouz, A.; Lamnawar, K. Fluorinated ethylene propylene coatings deposited by a spray process: Mechanical properties, scratch and wear behavior. *Polymers* **2022**, *14*, 347. [CrossRef]
11. Chen, K.; Xiao, C.; Huang, Q.; Liu, H.; Liu, H.; Wu, Y.; Liu, Z. Study on vacuum membrane distillation (VMD) using FEP hollow fiber membrane. *Desalination* **2015**, *375*, 24–32. [CrossRef]
12. Hirschmann, B.; Oreski, G.; Pinter, G. Thermo-mechanical characterisation of fluoropolymer films for concentrated solar thermal applications. *Sol. Energy Mater. Sol. Cells* **2014**, *130*, 615–622. [CrossRef]
13. French, R.H.; Rodríguez-Parada, J.M.; Yang, M.K.; Derryberry, R.A.; Pfeiffenberger, N.T. Optical properties of polymeric materials for concentrator photovoltaic systems. *Sol. Energy Mater. Sol. Cells* **2011**, *95*, 2077–2086. [CrossRef]
14. Drobny, J.G.; Ebnesajjad, S. *Technology of Fluoropolymers: A Concise Handbook*, 3rd ed.; CRC Press: Boca Raton, FL, USA, 2023; pp. 27–129.
15. Zhang, L.; Wang, H.; Li, Y. Effects of annealing on the crystallinity and mechanical properties of FEP films. *Polym. Eng. Sci.* **2022**, *62*, 3215–3223.
16. Lee, J.; Kim, S. Thermal surface activation of FEP films for enhanced adhesion. *J. Fluor. Chem.* **2021**, *250*, 109929.
17. Chen, W.; Xu, D.; Zhao, Y. Surface modification of FEP films by UV/ozone treatment for enhanced adhesion. *Surf. Coat. Tech.* **2023**, *460*, 129526.
18. Patel, A.R.; Nguyen, T.; Garcia, M. Photografting of hydrophilic monomers onto FEP substrates via UV activation. *J. Appl. Polym. Sci.* **2021**, *138*, e50412.
19. Matsumoto, K.; Tanaka, Y.; Hirose, T. Surface structuring of FEP films by UV-laser processing for microfluidic applications. *ACS Appl. Mater. Interfaces* **2024**, *16*, 1870–1880.
20. Singh, R.; Thomas, J.P.; Seo, Y. Synergistic effects of heat and UV treatments on the surface properties of FEP films. *Mater. Chem. Phys.* **2023**, *299*, 127445.
21. Augulis, L.; Tamulevičius, S.; Augulis, R.; Bonneville, J.; Goudeau, P.; Templier, C. Electronic speckle pattern interferometry for mechanical testing of thin films. *Opt. Lasers Eng.* **2004**, *42*, 1–8. [CrossRef]
22. Augulis, L.; Tamulevičius, S.; Bonneville, J.; Templier, C.; Goudeau, P. Testing of the mechanical properties of thin films: A review. *Mater. Sci.-Medzg.* **2002**, *8*, 3–8.
23. Liu, J.M. Simple technique for measurements of pulsed Gaussian-beam spot sizes. *Opt. Lett.* **1982**, *7*, 196–198. [CrossRef] [PubMed]

24. Jee, Y.; Becker, M.F.; Walser, R.M. Laser-induced damage on single-crystal metal surfaces. *J. Opt. Soc. Am. B* **1988**, *5*, 648–659. [CrossRef]
25. Holzwarth, U.; Gibson, N. The Scherrer equation versus the 'Debye-Scherrer equation'. *Nat. Nanotechnol.* **2011**, *6*, 534. [CrossRef] [PubMed]